Geochemical records reveal protracted and differential marine redox change associated with Late Ordovician climate and mass extinctions

Nevin P. Kozik[1]*, Benjamin C. Gill[2], Jeremy D. Owens[1], Timothy W. Lyons[3], and Seth A. Young[1]

[1] Department of Earth, Ocean, and Atmospheric Science and National High Magnetic Field Laboratory, Florida State University, Tallahassee, Florida, 32306, USA

[2] Department of Geosciences, Virginia Polytechnic Institute and State University, Blacksburg, Virginia, USA

[3] Department of Earth and Planetary Sciences, University of California, Riverside, CA, USA

Corresponding author: Nevin Kozik (nkozik@fsu.edu)

Key Points:

- Newly paired iodine and sulfur geochemistry highlight the role of shelf anoxia during the Late Ordovician Mass Extinction.
- Iodine records show pervasive local anoxia, while sulfur records reveal waning then waxing sulfidic conditions in Late Ordovician oceans.
- A combination of reducing marine conditions, climatic cooling, and glacioeustacy caused the first mass extinction in the Phanerozoic.

Abstract

The Ordovician (Hirnantian; 445 Ma) hosts the second most severe mass extinction in Earth history, coinciding with Gondwanan glaciation and a growing body of geochemical evidence for marine anoxia. It remains unclear whether global cooling, expanded oxygen-deficiency, or a combination drove the Late Ordovician Mass Extinction (LOME). Here, we present new paired iodine and sulfur isotope geochemical data from three globally distributed carbonate successions to constrain changes in local and global marine redox conditions. Iodine records suggest locally anoxic conditions were potentially pervasive on shallow carbonate shelves, while sulfur isotopes suggest a reduction in global euxinic (anoxic and sulfidic) conditions. Late Katian sulfate-sulfur isotope data show a large negative excursion that initiated during elevated sea level and continued through peak Hirnantian glaciation. Geochemical box modeling suggests a combination of decreasing pyrite burial and increasing weathering are required to drive the observed negative excursion. This reduction of pyrite burial suggests a ~3% decrease of global seafloor euxinia during the Late Ordovician. The sulfur datasets spanning the late Hirnantian–early Silurian provide further evidence that this trend was followed by increases in euxinia which coincided with eustatic sea-level rise during subsequent deglaciation. A persistence of shelf anoxia against a backdrop of waning then waxing global euxinia was linked to the two LOME pulses. These results place important constraints on both local and global marine redox conditions throughout the Late Ordovician and suggest that non-sulfidic shelfal anoxia—along with glacioeustatic sea level and climatic cooling—were important factors leading to the LOME.

Plain Language Summary

Changes in ocean oxygen contents have had major impacts on marine biodiversity since the rise of animals 600 million years ago. Here we use paired iodine concentrations and sulfur isotope data to constrain paleoredox conditions surrounding the Late Ordovician Mass Extinction (LOME; ~445 Ma), the second-largest mass extinction in Earth history, and the only of the “Big 5” that occur during icehouse conditions. Despite previous work, the role of oxygen deficiency during the LOME remains controversial and under constrained. This study is the first multi-basinal and multiproxy datasets to specifically reconstruct local and global marine redox conditions surrounding the two LOME pulses. These results suggest that a unique and vacillating combination of anoxic and euxinic (anoxic and sulfidic water column) marine conditions. Thus, redox variability tied with climatic cooling, and glacioeustacy

45 were potential mechanisms leading to the first mass extinction in the Phanerozoic.

47

48 Introduction

49 The Early Paleozoic, notably the Ordovician Period, hosts one of the largest marine biodiversification
50 events in Earth history, the Great Ordovician Biodiversification Event (GOBE). Not long after this proliferation of
51 marine fauna, however, the second-largest mass extinction in Earth history occurred, the Late Ordovician Mass
52 Extinction Event (LOME; (Harper et al., 2014)). The LOME resulted in the loss of ~85% of marine species during
53 two distinct extinction pulses, with the first occurring at the Katian-Hirnantian boundary, and the second in the late
54 Hirnantian (Brenchley et al., 2001; Harper et al., 2014). Traditionally, the first LOME pulse has been associated
55 with rapid global cooling and widespread glaciation that resulted in major eustatic sea-level fall, creating widespread
56 marine habitat loss and ecologic shifts (Harper et al., 2014). The second LOME pulse has been associated with sea-
57 level rise and an expansion of anoxic (potentially euxinic, anoxic, and sulfidic water column) conditions
58 (Hammarlund et al., 2012). However, recent studies have invoked widespread anoxia/euxinia for both LOME
59 pulses, indicating that the redox conditions surrounding this event might be more complex than initially understood
60 (Zou et al., 2018). Associated with the LOME was a major perturbation in the global carbon cycle, recorded as a
61 positive excursion in the marine carbon isotope record known as the Hirnantian carbon isotope excursion (HICE)
62 (Brenchley et al., 2003).

63 The primary causal mechanisms for the HICE has previously been attributed to changes in carbonate
64 weathering regimes during eustatic sea-level fall (Kump et al., 1999) and/or enhanced burial of organic matter
65 associated with increased preservation resulting from decreased marine oxygenation (Brenchley et al., 2003;
66 Hammarlund et al., 2012; Jones and Fike, 2013). Traditional sulfur (S) isotope approaches have investigated the
67 dynamics and extent of euxinic marine conditions during the LOME. Pyrite sulfur isotope ($\delta^{34}S_{pyr}$) profiles across
68 multiple globally distributed paleobasins show nearly synchronous positive excursions, suggesting a global
69 perturbation, albeit with local overprints to explain the variable magnitudes ~15-40‰. Overall, the positive $\delta^{34}S_{pyr}$
70 shift may reflect increased pyrite burial under widespread sulfidic conditions (Hammarlund et al., 2012; Jones and
71 Fike, 2013). However, the single reported seawater sulfate ($\delta^{34}S_{CAS}$) record shows little variation in this global redox

proxy throughout the HICE, suggesting a minimal change in global pyrite burial rates over this interval and thus a limited global expansion of euxinic conditions (Jones and Fike, 2013).

Additionally, non-traditional paleoredox proxies have been applied to assess the extent of widespread reducing conditions as a potential kill mechanism for both LOME pulses. Specifically, uranium and molybdenum ($\delta^{238}U$ and $\delta^{98}Mo$) stable isotope records have been interpreted to reflect global to regional changes in marine redox, and have identified possible shifts towards more reducing conditions—but at differing times during the Hirnantian (Zhou et al., 2015; Bartlett et al., 2018). Models based on $\delta^{238}U$ data from eastern Laurentia suggest up to 15% of the total seafloor area experienced anoxic conditions just before the end of the Ordovician (Bartlett et al., 2018). Meanwhile, $\delta^{98}Mo$ data from South China have been interpreted to record local shifts from suboxic to euxinic conditions prior to and during the early Hirnantian (Zhou et al., 2015). However, each of these marine redox interpretations are based on singular datasets within widely different depositional environments. Moreover, delineating the timing of these inferred changes in redox relative to one another remains problematic, as the lack of a universally accepted, fully integrated Upper Ordovician biostratigraphic scheme limits the resolution of correlations (see supplemental information). Additionally, these two paleoredox proxies have different specific responses due to their position on the redox ladder, i.e. changes in increasingly reducing marine conditions, which creates additional complications for understanding the onset of non-sulfidic anoxia ($\delta^{238}U$) versus euxinia ($\delta^{98}Mo$).

To better elucidate critical gaps in our understanding of the mechanistic underpinnings for the LOME, we present new I/(Ca+Mg) ratios and $\delta^{34}S_{CAS}$ datasets from three widely distributed Upper Ordovician carbonate successions. Our study localities were deposited in different paleocean basins and record the HICE along with major fluctuations in eustatic sea level (Finney et al., 1997; Young et al., 2010; Ghienne et al., 2014; Kiipli and Kiipli, 2020). These new-paired geochemical datasets provide a more comprehensive understanding and specificity of marine redox conditions (local and global) and climate that led to the second-largest extinction event in Earth history.

2. Background

2.1 Geologic setting

Epeiric seaways were widespread throughout much of the Late Ordovician as a result of elevated eustatic sea levels (Rasmussen et al., 2019). Widespread carbonate deposition dominated these epeiric seaways with carbonate successions found even in mid-latitude settings such as the paleocontinent of Baltica (Fig. 1).

100 Subsequently, nearly every marine setting records a major decrease in sea level during the latest Katian and
101 Hirnantian marked by subaerially exposed carbonate platforms and significantly reduced shallow-water marine
102 habitats.

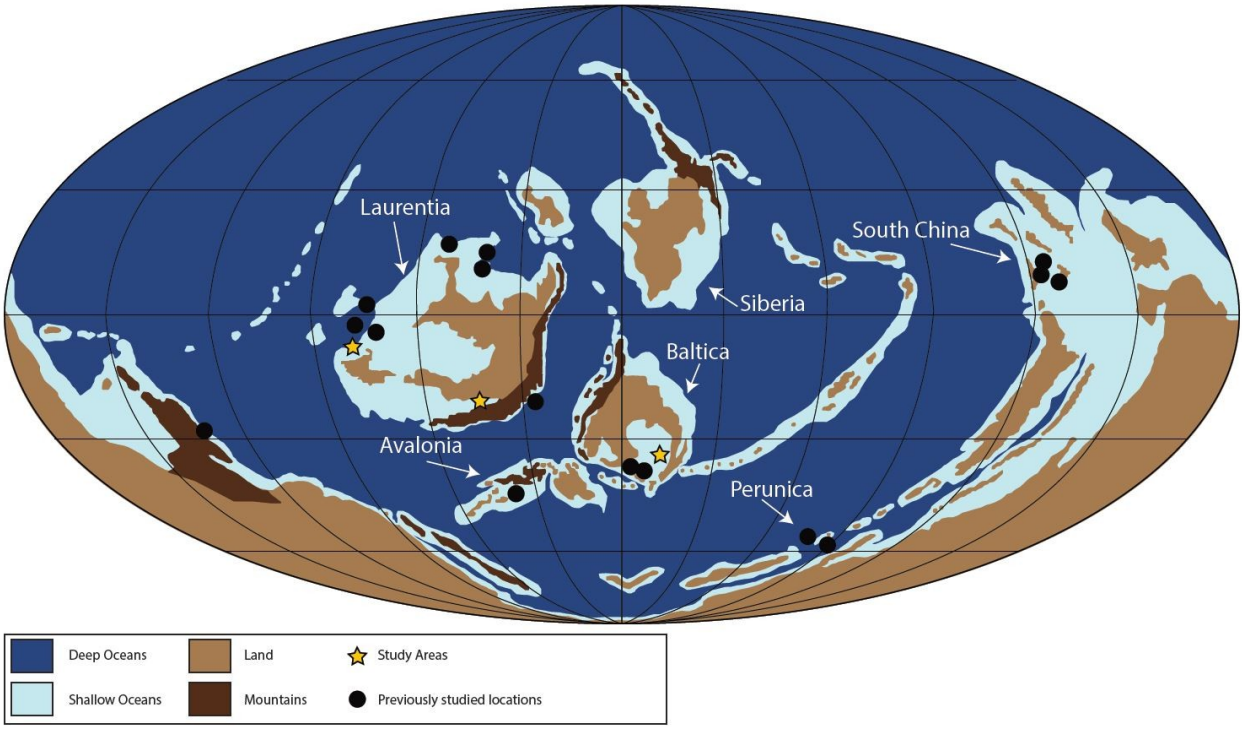

Figure 1. Paleogeographic reconstruction of the Late Ordovician. Modified from Melchin et al., 2013. Study site localities are marked as yellow stars, with the locations of other study areas shown in black circles.

The first study site is a thick succession outcropping in the Monitor Range, Nevada, where high-resolution $\delta^{13}C_{carb}$ records have previously documented the HICE (Finney et al., 1997, 1999; Jones et al., 2016). This section consists of the Late Ordovician Hanson Creek Formation as well as the early Silurian Roberts Mountain Formation (Finney et al., 1997). These marine carbonates were deposited in an upper slope setting on the western passive margin of Laurentia in the Panthalassic Ocean and contain facies that range from deep water thinly laminated lime mudstones and bedded cherts to wave agitated cross-laminated oolitic grainstones (Finney et al., 1997). The second study site is a thick succession recorded within the Kardla drill core, southern Estonia consisting of the Late Ordovician Jonstrop, Halliku, Kuldiga, and Saldus formations, and the early Silurian Õhne Formation (Kaljo et al., 2001). These carbonates were deposited along the southern margin of Baltica with direct connection to the Iapetus Ocean and contain facies ranging from offshore argillaceous wackestones to shallow water oolitic grainstones (Kiipli and Kiipli, 2020). Last, the Pointe Laframboise section on Anticosti Island, Quebec, contains the Late Ordovician Ellis Bay and early Silurian Becscie formations. This is a mixed siliciclastic and carbonate succession

deposited on a storm-dominated carbonate ramp in a foreland basin on eastern Laurentia (Desrochers et al., 2010). Facies range from distal bioturbated mudstones through shallow patch reef limestones. Each of our study localities has been the subject of extensive biostratigraphic and $\delta^{13}C_{carb}$ chemostratigraphic studies, allowing for correlation between the sections (supplemental material Fig S1).

However, detailed correlations of stratigraphic sections from hydrographically separate paleobasins remain difficult in any study, especially when comparing sections with biostratigraphic zonation based on different taxonomic groups. Here we base our Late Ordovician–Early Silurian stratigraphic correlations on available graptolite, conodont, and chitinozoan biostratigraphy, as well as the high-resolution $\delta^{13}C_{carb}$ trends. The Monitor Range section contains diagnostic Late Ordovician graptolites (e.g., *Metabolograptus extraordinarius* and *Metabolograptus persculptus* biozones) and conodonts (*Amorphoganathus ordovicicus* biozone) (Murphy et al., 1979; Finney et al., 1997, 1999), which provide direct and reliable high-resolution integration of this section with the latest calibrated Ordovician Time Scale-2020 (Goldman et al., 2020). The other sections, western Anticosti Island and the Kardla drill core, contain diagnostic conodonts and chitinozoan biozones (Brenchley et al., 2003). Both sections contain the chitinozoan *Belonechitina gamachiana* and *Spinachitina taugourdeaui* biozones, allowing for precise correlation between these two localities. Because of the lack of a common biostratigraphic scheme, we also rely on the carbon isotope stratigraphy previously documented from each study site to augment some issues in integrating differing biostratigraphic schemes from these three successions (see supplemental materials for more information).

2.2. Local and global redox proxies

Iodine-to-calcium (I/Ca+Mg) ratios in carbonate minerals are thought to capture local changes in water column oxygen contents (Lu et al., 2010). When discussing concentration patterns, iodine abundances are normalized to carbonate contents and magnesium (Mg) concentrations are included to account for varying carbonate mineralogy (Hardisty et al., 2014, 2017; Lu et al., 2018). Although iodine has a relatively long residence time in the modern ocean (~300 kyr), iodine responds rapidly to changes in local reducing conditions due to its redox potential (Rue et al., 1997; Hardisty et al., 2020). Under well-oxygenated local conditions, iodate (IO_3^-) is the dominant species of iodine, while under reducing conditions iodate is converted to iodide (I^-) (Rue et al., 1997). The redox potential of iodate to iodide is similar to that of O_2, Mn^{2+}, and NO_3^-, thus high iodate concentrations (>2.6 μmol/mol) tend to correlate with well-oxygenated portions of the modern surface oceans and predictably decrease in oxygen

147 minimum zones (OMZs; 0.5–2.5 μmol/mol) (Rue et al., 1997; Lu et al., 2010). Within this framework,
148 concentrations of iodate within carbonate minerals can be used to track local paleoredox conditions, as iodate readily
149 substitutes for the carbonate ion, while iodide is excluded from the lattice structure (Lu et al., 2010). Furthermore,
150 iodine has a higher reduction potential than more widely used U, Mo, and S proxies and thus responds more readily
151 to low-oxygen conditions (Lu et al., 2010).

152 Sulfate-S isotope compositions and concentrations in the global oceans are controlled by the input and
153 output fluxes of sulfur to and from the oceans. The two major input fluxes are riverine sulfate and volcanic
154 outgassing, which have a combined value of 1.5×10^{18} mol/Myr, and both have isotopic compositions that range
155 between 0‰ to +9‰ (Burke et al., 2018). Important output fluxes for sulfur are the burial of sulfate-evaporites,
156 which carries a small isotopic fractionation and a flux of 0.83×10^{18} mol/Myr, and sedimentary pyrite with a flux of
157 0.67×10^{18} mol/Myr (Burke et al., 2018). Pyrite formation via microbial sulfate reduction (MSR) records up to a
158 70‰ sulfur isotope fractionation between sulfate and the product sulfide (approximated by $\Delta^{34}S$; $\Delta^{34}S = \delta^{34}S_{SO4} - \delta^{34}S_{H2S}$) (Lang et al., 2020; Pasquier et al., 2021). This process occurs in anaerobic environments and is dependent on
160 the availability of labile organic matter, reactive iron, and sulfate (Gomes and Hurtgen, 2015; Sim, 2019). Sulfur
161 isotopes of carbonate-associated sulfate ($\delta^{34}S_{CAS}$) are commonly used to generate high-resolution spatiotemporal
162 records of global marine sulfate-sulfur isotope compositions. Since marine sulfate throughout the Phanerozoic had a
163 significantly longer residence (10^5–10^7 yrs) time than inter-ocean mixing timescales (10^3 yrs) and thus is
164 homogenous throughout ocean basins, $\delta^{34}S_{CAS}$ values are generally representative of the global seawater reservoir.
165 Pyrite sulfur ($\delta^{34}S_{pyr}$) isotopes, in contrast, are best used as a local proxy for MSR activity and the associated factors
166 that control the magnitude of fractionation, such as rates of sulfate reduction, iron availability for pyrite formation,
167 and interplays between open and closed system dynamics (Lang et al., 2020; Pasquier et al., 2021).
168

169 3. Materials and methods

170 Weathered surfaces, when present, were removed from samples via a water-cooled saw to ensure the fresh
171 material was utilized for geochemical analysis. In-depth details regarding sample processing and purification for
172 carbonate-associated sulfate (CAS), pyrite sulfur, and I/(Ca+Mg) are described in the supplemental methods section.

Extracted CAS precipitated as $BaSO_4$ and sedimentary pyrite as Ag_2S were weighed into tin capsules with excess V_2O_5 and analyzed for their $\delta^{34}S$ values using a ThermoFisher Delta V at the University of California Riverside or a Finnigan MAT 252 at Indiana University. All sulfur isotopic ratios are reported in standard per mil (‰), using delta notation (δ) relative to Vienna Canyon Diablo Troilite (V-CDT) with reproducibility for all sulfur analyses better than ±0.2‰ based on replicates of the samples and standards. Standards used for sulfur isotopic analysis include the international standards NBS-127 =21.1‰; IAEA S-1 = -0.30‰; IAEA S-2 = 22.7‰; IAEA S-3 = -32.3‰; and EMR-CP = 1.07‰ an internal lab standard at Indiana University. I/(Ca+Mg) ratios were analyzed using an Agilent 7500cs inductively coupled-plasma mass spectrometer (ICP-MS) at the National High Magnetic Field Laboratory at Florida State University following standard methods (Lu et al., 2010). Internal standard curves were made fresh daily from high purity standards and compared to in-house and previously published geo-standards KL 1-2 and KL 1-4 from Hardisty et al., (2017) and were found to be within ±0.5% of the reported value. The precision of duplicate samples and replicate analysis were within ±0.08 μmol/mol or better.

4. Results

4.1 Monitor Range, Nevada, USA

Detailed carbon isotope data have been published from the Monitor Range section, documenting the HICE and other minor excursions (Murphy et al., 1979; Finney et al., 1999; Jones et al., 2016). The new I/(Ca+Mg) ratios from this section show relatively low values throughout the Katian and Hirnantian (Fig. 2), with average values in the *Dicellograptus ornatus* graptolite biozone at ~1.5 μmol/mol, declining to 0 μmol/mol in the *Paraorthograptus. pacificus* to *Diceratograptus murnis* biozones, and remaining at 0 μmol/mol to the uppermost part of the section where values rise to an average of ~1.5 μmol/mol. $\delta^{34}S_{CAS}$ data from this section show an average of +36‰ throughout much of the lower Hanson Creek Formation, with a protracted fall beginning in the late Katian *D. ornatus* biozone and reaching minimum values of +26‰ in the early Hirnantian *M. extradinarious* biozone. Within the late Hirnantian *M. persculptus* biozone, $\delta^{34}S_{CAS}$ values increase to an average of +29‰ and continue to increase to +35‰ in the Silurian Rhuddanian *Distomodus kentuckyensis* conodont biozone.

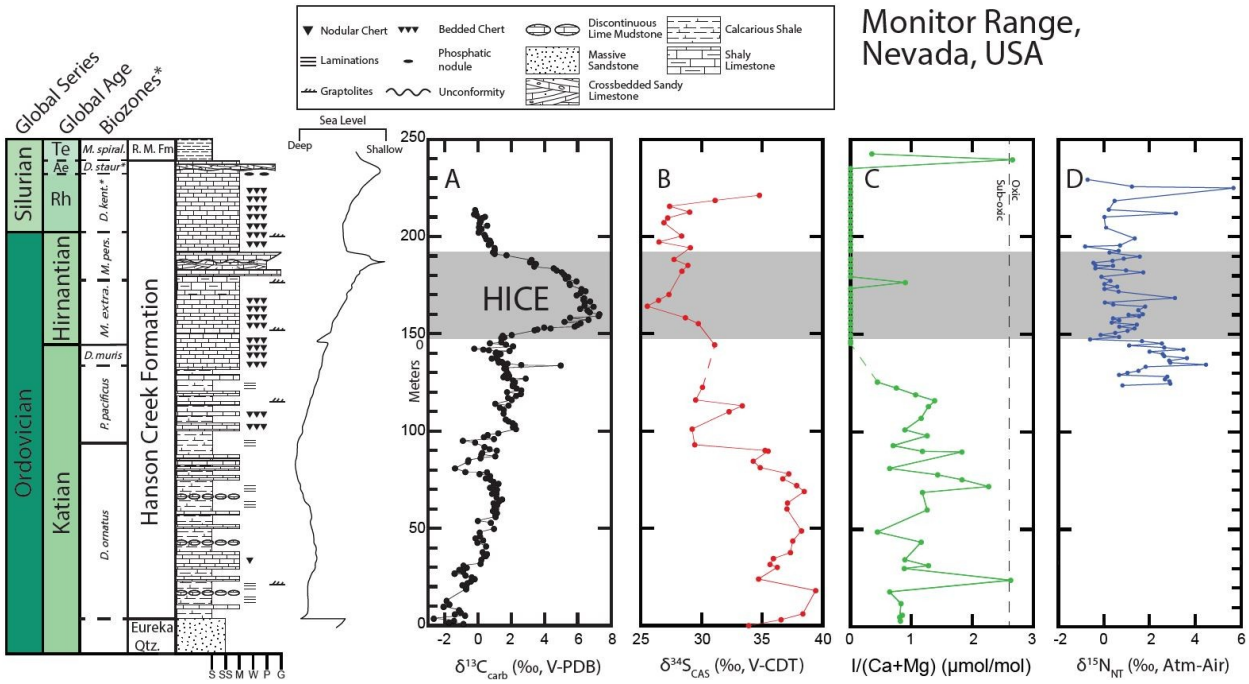

Figure 2. Geochemical and lithologic profile of Monitor Range, Nevada. Biozones, lithologic profile and sea level curve are from Finney et al., 1997, 1999 and Murphy et al., 1979 (* indicates conodont biozone). A) $\delta^{13}C_{carb}$ replotted from Jones et al., 2016. B) $\delta^{34}S_{CAS,}$ this study. C) I/(Ca+Mg) ratios, this study. D. $\delta^{15}N_{NT}$ replotted from LaPorte et al., 2009 *.D. kent.** = *D. kentuckyensis*, *D. staur.** = *D. staurognathoides* R.M. Fm = Roberts Mountains Formation.

4.2 Kardla drill core, Estonia

A detailed carbon isotope record has also been published from the Kardla core, Estonia, where the HICE was also identified (Kaljo et al., 2001; Young et al., 2010). The I/(Ca+Mg) values within the upper Halliku Formation show a consistent absence of iodine (0 µmol/mol) but begin to increase within the Kuldiga Formation (*Conochitina scabra* biozone) to a maximum value of 1.6 µmol/mol. The values fall to near zero (< 0.1 µmol/mol) at the top of the formation (Fig. 3). Iodine contents increase again within the Saldus Fm to a maximum of 1.5 µmol/mol and then decline to near-zero values within the basal Õhne Formation. Finally, I/(Ca+Mg) ratios increase steadily throughout the Õhne Formation (*Spinachitina fragilis* biozone) to a maximum of 2 µmol/mol. The $\delta^{34}S_{CAS}$ data from the Kardla core show a negative perturbation in the lowermost Halliku Formation, within the Katian lower *Conochitina rugata* chitinozoan biozone, from maximum values of +30‰ to minimum values of +20‰. Subsequently, $\delta^{34}S_{CAS}$ values remain relatively invariant, ranging between +20‰ to +25‰ into the Hirnantian (late *C. rugata* through *S. scabra* biozones), where average values trend to +30‰ in the upper Kuldiga through Õhne formations (S. *fragilis* biozone). The corresponding $\delta^{34}S_{pyr}$ values range between -35‰ and +7‰, with an average of

~ -17‰ within the Halliku Formation. The overlying Kuldiga and Saldus formations record $\delta^{34}S_{pyr}$ values that steadily increase to a maximum value of +37‰, and these values return to a new baseline of ~ -30‰ in the overlying Õhne Formation.

Figure 3. Geochemical and lithologic profile of the Kardla Drill Core, Estonia. Chitinozoan biozones and lithologies are modified from Kaljo et. al., 2001 and Young et. al., 2010. A) $\delta^{13}C_{carb}$ replotted from Young et. al., 2010. B) $\delta^{34}S_{CAS}$ this study. C) $\delta^{34}S_{pyr}$ this study. D) $\Delta^{34}S$, this study. E) I/(Ca+Mg) ratios, this study.

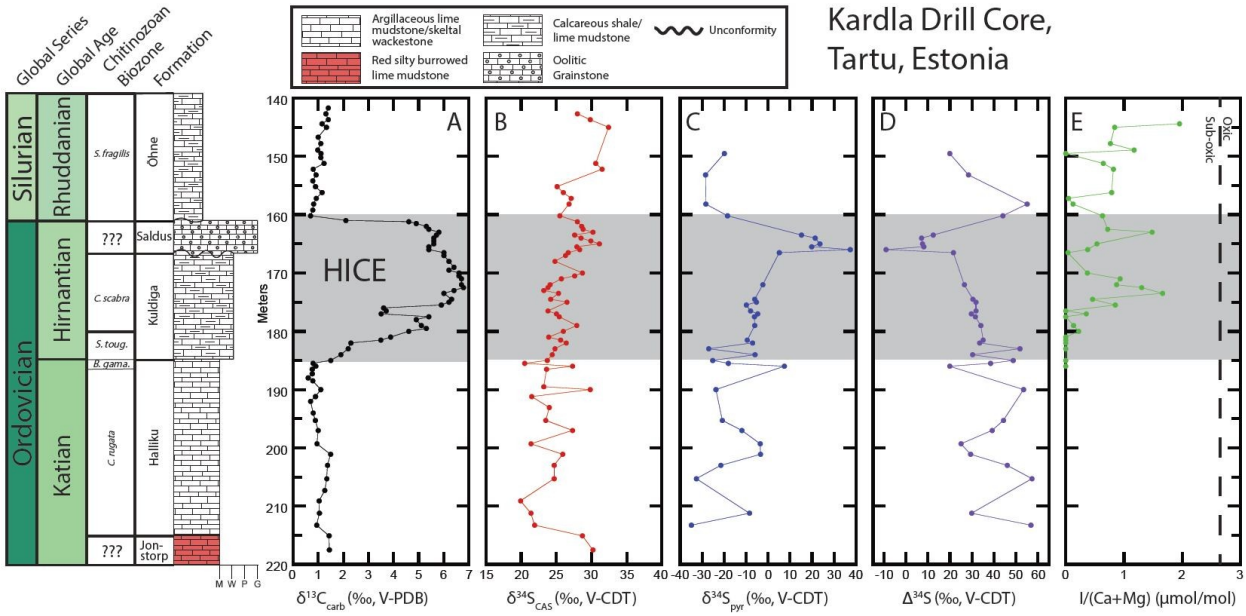

4.3 Anticosti Island, Canada

The Point Laframboise section on western Anticosti Island has been studied extensively, including previously published geochemical data for carbon, sulfur, and uranium isotopes in addition to carbonate clumped- and conodont palaeothermometry (Finnegan et al., 2011; Jones et al., 2011; Jones and Fike, 2013; Bartlett et al., 2018). Previous studies have documented the HICE in detail from this section in addition to cooling trends in sea-surface temperatures and increases in global marine anoxia. Our new I/(Ca+Mg) dataset (Fig. 4) from the same section shows low values (< 2 µmol/mol) within the *B. gamachiana* and *S. taugrourdeaui* biozones of the mid-inner ramp facies of the Lousy Cove Member, but values increase rapidly to an average of 6 µmol/mol, ranging from ~0.5 to 9 µmol/mol, within the patch reef facies of the Laframboise Member. Subsequently, I/(Ca+Mg) ratios within the early Silurian inner-mid ramp carbonates of the overlying Becscie Formation (*Ancyrochitina ellisbayensis* and *Plectochitina nodifera* biozones) show a return to consistently low values (< 1 µmol/mol).

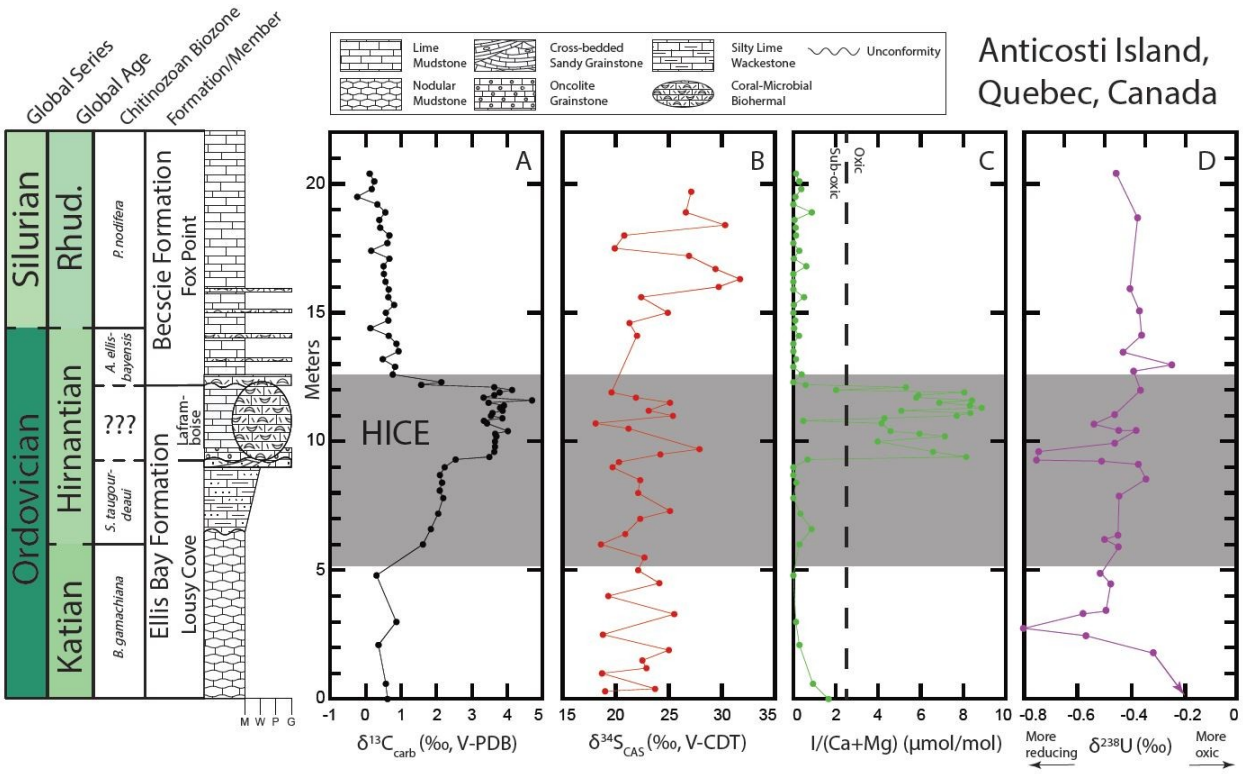

Figure 4. Geochemical and lithologic profile of Anticosti Island, Canada. Chitinozoan biozones and lithologies are modified Jones and Fike 2013. A) $\delta^{13}C_{carb}$ replotted from Young et al., 2010. B) $\delta^{34}S_{CAS}$ replotted from Jones and Fike 2013. C) I/(Ca+Mg) ratios, this study. D) $\delta^{238}U$ replotted from Bartlett et al., 2018.

5. Discussion

5.1 Evaluation of diagenetic influences

Assessing I/(Ca+Mg) and $\delta^{34}S_{CAS}$ values for potential diagenetic overprints is paramount to ensure the recorded signals represent changes in seawater. Importantly, a recently published study using $\delta^{44}Ca$ and Sr/Ca ratios addressed the extent of diagenetic influence on both the Monitor Range and western Anticosti Island sections (Jones et al., 2020). This study suggests that deeper water settings like that of Monitor Range and western Anticosti Island, generally retain primary seawater geochemical signatures (i.e. sediment buffered), while strata deposited in shallower water settings are more likely to reflect geochemical signatures akin to sediment porewaters (Jones et al., 2020). Unfortunately, extensive diagenetic studies have not been performed on the Kardla drill core, Estonia, however this section is interpreted to be deposited in a deeper shelf setting (albeit shallower than the upper slope

setting of the Monitor Range section), suggesting that this section likely preserves mostly primary geochemical signatures (Kaljo et al., 2011).

Meteoric diagenesis has been shown to decrease the concentrations of both iodine (Lu et al., 2010; Hardisty et al., 2017) and sulfate in carbonates, as freshwater typically contains lower concentrations of these ions. However, there are no known processes that can increase iodine in carbonates, and in the case of CAS, meteoric diagenesis itself imparts a negligible isotopic effect (Gill et al., 2008), however early diagenetic processes can still impart isotopic signatures. While there is an abundance of low I/(Ca+Mg) values recorded in our datasets, we interpret these as predominantly primary seawater signatures as significant diagenetic alteration cannot explain the very high I/(Ca+Mg) ratios, some of the highest in the early Paleozoic (Lu et al., 2018), recorded within the shallow marine patch reef facies of the western Anticosti Island section. These high I/(Ca+Mg) values were recorded during a lower stand of sea level in the Hirnantian, a stratigraphic interval, and carbonate facies that would have been most susceptible to extensive diagenesis (Fig. SI 3B). Studies of Cenozoic carbonates from the Great Bahamas Bank have shown that iodine concentrations may also be reduced during early diagenesis in carbonate settings (Hardisty et al., 2017). Intervals that were affected by meteoric diagenesis contained I/(Ca+Mg) values close to 0 μmol/mol (Hardisty et al., 2017), likely reflecting alteration by reducing fluids rather than primary seawater values. While it is possible that processes similar to these may have contributed to lowering general iodine concentrations in carbonates from this study, if fluid migration were to greatly affect primary geochemical signals it would be in the units that would have originally contained the highest porosity and lowest permeability (i.e. the shallow-water facies). In other words, the Lamframboise Member–Ellis Bay Formation, Anticosti Island and the Saldus Formation, Estonia, by this prediction would have low I/(Ca+Mg) values. However, these respective intervals within our carbonate successions contain the highest I/(Ca+Mg) values, while the lowest values are found in fine-grained carbonate and clay-rich facies where porosity and permeability would have likely inhibited fluid migration. Additionally, these Bahamian drill cores have shown other evidence for meteoric diagenesis in these intervals with near zero I/(Ca+Mg) values, including carbon isotopic signatures that are significantly depleted compared to the original aragonitic sediments that passively record primary seawater (Swart and Oehlert, 2018), whereas the Late Ordovician carbon isotopic data from our study sections do not show these types of signatures even surrounding intervals of glacioeustatic exposure (Brenchley et al., 2003; Desrochers et al., 2010; Young et al., 2010; Jones et al., 2016).

Geochemical crossplots are also a widespread tool used to assess the fidelity of geochemical signatures, where correlating trends with high R^2 values can point to mixing of primary marine signal with those from diagenetic alteration. Recrystallization of carbonates during diagenesis can yield $\delta^{13}C$, $\delta^{18}O$, $\delta^{34}S$ and I/(Ca+Mg) signatures that deviate from primary seawater values, reflecting a mixture of primary and secondary sources and producing linear or asymptotic relationships among the geochemical parameters (Ahm et al., 2018; Swart and Oehlert, 2018). Here we have cross-plotted $\delta^{18}O_{carb}$, $\delta^{13}C_{carb}$, [CAS], $\delta^{34}S_{CAS}$, and I/(Ca+Mg) datasets, and show weak to no correlations, indicating that complete diagenetic overprint is absent from our datasets (supplemental material, Fig. S3). The only crossplots that show significant correlation are I/(Ca/Mg) vs $\delta^{18}O_{carb}$ and $\delta^{18}O_{carb}$ vs $\delta^{13}C_{carb}$ from Anticosti Island, however, these trends simply reflect two distinct data populations that internally do not correlate. Further, clear trends that continue across formational boundaries and major facies changes suggest that geochemical signatures found in these successions are largely primary and contain limited diagenetic alteration.

The likelihood of bulk CAS to faithfully record primary seawater sulfur isotope values has previously been called into question. Bulk $\delta^{34}S_{CAS}$ may incorporate sulfate from both primary and secondary carbonate phases potentially leading to more "noise" in isotopic datasets, while $\delta^{34}S_{CAS}$ from well-preserved brachiopod carbonate components in the same section show more invariant values (Present et al., 2015). Unfortunately, brachiopods within the sections presented here are relatively rare and thus not a viable option for performing high-resolution component-specific CAS measurements. Studies comparing early Cenozoic bulk CAS, planktonic foraminiferal CAS, and authigenic barite found that while species-specific foraminiferal data yielded vital effects up to ±1‰ versus barite, bulk CAS faithfully follow the recorded changes in secular $\delta^{34}S_{sulfate}$ in both duration and magnitude (Toyama et al., 2020; Yao et al., 2020). Additionally, $\delta^{34}S_{CAS}$ records presented here across multiple paleobasins on separate paleocontinents from variable bathymetric depths show biostratigraphically, well correlated first-order trends (i.e. the fall $\delta^{34}S$ in the late Katian and a return to heavier values within the late Hirnantian–Rhuddanian) also suggest preservation of primary seawater signatures (Fig. 5). While local diagenetic processes have may influenced the $\delta^{34}S_{CAS}$ data, it is very unlikely that each of the study sections would experience similar early and late diagenetic histories that resulted in similar first-order trends. These local diagenetic histories can more likely explain the smaller magnitude variations (~2-4‰) within and between $\delta^{34}S_{CAS}$ records from the study sites.

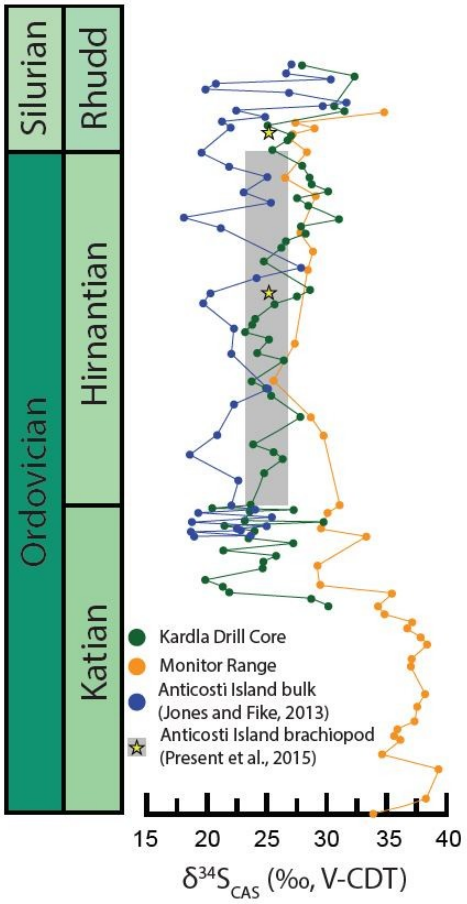

Figure 5. Comparison of new Late Ordovician–Silurian $\delta^{34}S_{CAS}$ datasets from this study and those previously published (Jones and Fike, 2013; Present et al., 2015). Note the clear overlap in $\delta^{34}S_{CAS}$ values from bulk- and brachiopod-carbonate throughout the Hirnantian. Approximate chronostratigraphic locations of brachiopod component CAS samples are marked as yellow stars.

5.2 Modeling the sulfur cycle

Our $\delta^{34}S_{CAS}$ trends recorded from the Monitor Range documents an ~10‰ fall leading into the Hirnantian. The data are the base of the Kardla core appear to capture the very end of this fall and, when taken with the Monitor Range data, suggest this represents a global perturbation in the sulfur cycle. Here we constructed a forward sulfur isotope mass balance box model to reproduce the magnitude of the isotope perturbation and to provide quantitative constraints on global pyrite burial and weathering fluxes. We prescribed initial conditions based on modern estimates of weathering and pyrite burial rates (Kurtz et al., 2003), and sensitivity tests were explored for all fluxes (for initial parameters and values explored see SI Table 1). While this type of modeling cannot provide a single unique solution from the changes in the sulfur cycle, it does provide a range of plausible first-order quantifications for these various parameters. It is important to note that all model runs presented here (Fig. 6) were prescribed with

a change in the sulfur isotope fractionation ($\Delta^{34}S$). We start with an initial value of +35‰ and decrease it to +20‰ during the perturbation, consistent with a global average of previously published $\Delta^{34}S$ values (see supplemental material for more information, Table 2) and those determined in this study. The starting seawater sulfate-S isotope composition for the late Katian of ~ +35‰ is based on our $\delta^{34}S_{CAS}$ dataset from the Monitor Range. We have used recent Sr isotope weathering models for the Late Ordovician (Hu et al., 2017) and previously published Late Ordovician–Silurian global redox studies (Bartlett et al., 2018; Stockey et al., 2020) for further model constraints for changes in the pyrite burial flux. The time interval adopted for all model runs is 5 Myr for the duration of the negative $\delta^{34}S_{CAS}$ excursion based on graptolite biostratigraphy of the Monitor Range section that can be well integrated into the latest calibrated Ordovician Time Scale-2020 (Goldman et al., 2020; see supplemental material for more details on age constraints).

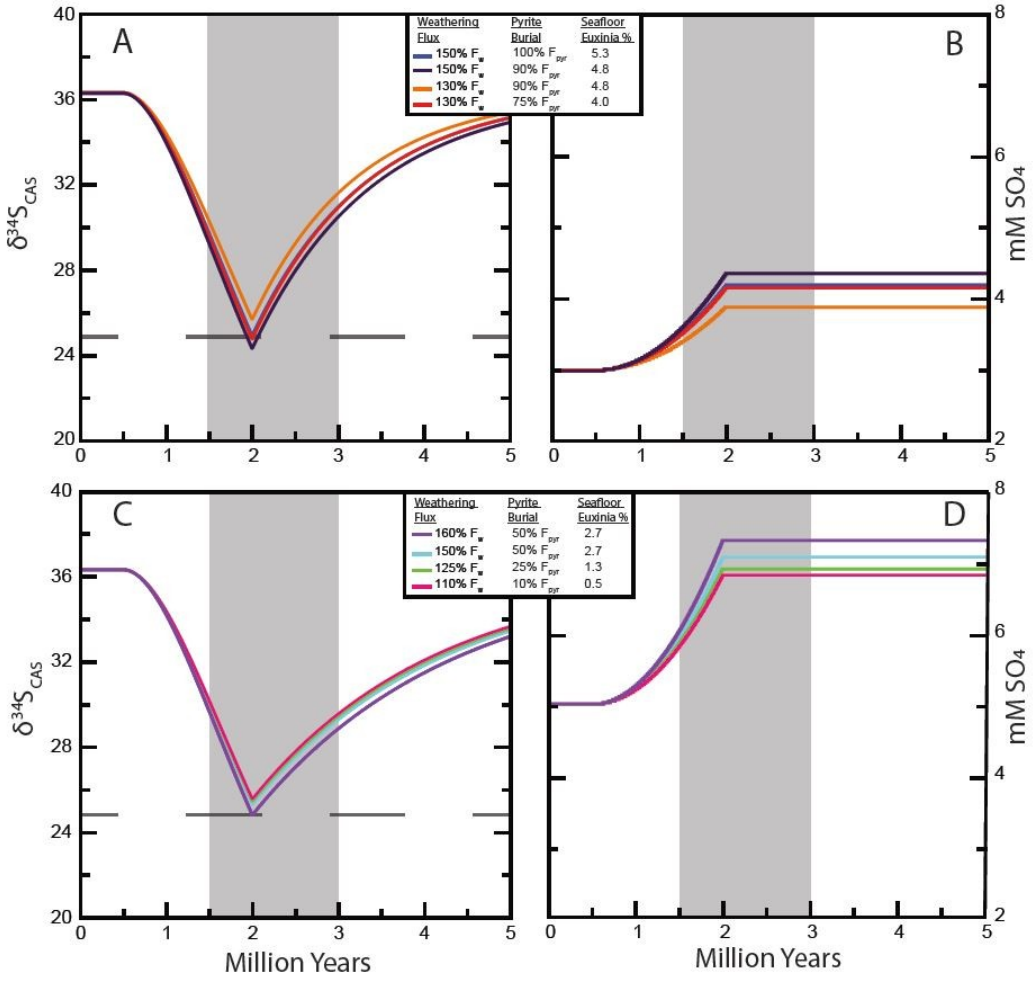

Figure 6. Results of geochemical box modeling showing changes in pyrite burial (F_{pry}), weathering fluxes (F_w) needed to reproduce seen CAS trends in Monitor Range for a 3mM SO_4^{-2} scenario (panels A and B) and a 5mM SO_4^{-2} scenario (panels C and D). Also shown are changes in sulfate concentrations resulting from the associated weathering and pyrite burial fluxes (panels B and D). Grey interval in all panels represents the HICE interval. For additional sensitivity tests, see supplemental materials.

Changes to any single model parameter were unable to reproduce the fall in $\delta^{34}S_{CAS}$ in the required timeframe (supplemental material). However, model runs assuming moderate decreases in pyrite burial in concert with an increase in weathering can generate the observed $\delta^{34}S_{CAS}$ drop (Fig. 6). A 50–75% reduction in pyrite burial (i.e. 50% F_{pyr} and 25% F_{pyr} of initial burial rate, respectively) combined with a 25–60% increase in the weathering flux (i.e., 125% F_w and 160% $F_{w,}$ respectively) produces a ~10‰ drop using an initial marine sulfate concentration of 5 mM. This scenario is the most parsimonious with the initiation of sea-level fall, which would reduce shelf area and thus the total aerial extent of pyrite burial, as well as increase the weathering inputs. This change in sea level is a result of changes in global climate and associated changes in thermohaline circulation at this time (see section 5.3 below) may have increased marine oxygenation of the Late Ordovician oceans, and further reduced global pyrite burial. These combined effects would both contribute to the observed $\delta^{34}S_{CAS}$ drop.

A starting marine sulfate concentration of 5 mM is consistent with previous estimates for Late Ordovician seawater (Horita et al., 2002; Jones and Fike, 2013). Model simulations starting with 3 mM marine sulfate concentrations require smaller changes in the weathering and pyrite burial fluxes (i.e., 25% reduction yields a value of 75% F_{pyr}) to simulate the negative excursion (Fig. 6A). However, we do not favor an initial marine sulfate concentration of 3 mM or less due since it is the low end of estimates based on fluid inclusions and previous Late Ordovician sulfur isotope modeling (Horita et al., 2002; Hammarlund et al., 2012; Jones and Fike, 2013). Furthermore, sensitivity tests with an initial 3 mM oceanic reservoir show changes in seawater sulfate sulfur isotopes that are faster than those documented from Upper Ordovician records in terms of reaching the minimum value and the later return to baseline. Additionally, our model places an upper constraint on Late Ordovician marine sulfate concentrations, as our simulations with initial values of 10 mM or greater cannot reproduce the observed sulfur isotope records unless unreasonable changes in weathering and pyrite burial fluxes are prescribed (supplemental material).

The observed negative $\delta^{34}S_{CAS}$ perturbation requires a major decrease in pyrite burial, thus potentially requiring a reduction in the global extent of euxinic conditions (since pyrite burial is highly efficient under such conditions).

As a thought experiment, if we assume that most pyrite is buried in euxinic settings, we can calculate a maximum estimate of euxinic seafloor area. This approach is an oversimplification since pyrite is also formed in reducing sediments overlain by oxic and anoxic non-sulfidic waters. However, since pyrite burial in these settings is less efficient, an even greater reduction in the area of the seafloor subject to reducing conditions is required. Initial pyrite burial flux for the late Katian required an F_{pyr} of 1.1×10^{18} mol of S/Myr, compared to the modern global rate of 0.67×10^{18} mol of S/Myr (Kurtz et al., 2003). The extent of euxinic conditions in the modern oceans is estimated at ~0.15% of the global seafloor (Reinhard et al., 2013), with reduced sulfur burial flux that would equate to $\sim 3.1 \times 10^{16}$ mol of S/Myr, most of which occurs in the Black Sea (Neretin et al., 2001). This reduced sulfur burial flux includes pyrite burial and any intermediate valence reduced S species, as well as organically bound S, and is thus a maximum estimate for reduced sulfur burial. Given this data from modern oceans and the estimated late Katian pyrite burial rates, we can estimate the extent of euxinic conditions in the late Katian at most was ~35× more than the modern, equating to an aerial extent of approximately 5.3% (35 × 0.15% of the modern). We estimate that a subsequent 75 to 50% reduction in pyrite burial—corresponding to the minimum $\delta^{34}S_{CAS}$ values—would reduce the maximum global estimate for the extent of euxinia to ~1.3 - 2.7% within the Hirnantian. We observe a shift back to heavier $\delta^{34}S_{CAS}$ values in the late Hirnantian-early Silurian, likely signaling a return to more reducing conditions with the oceans.

Due to the susceptibility of carbonate-associated sulfate data to be possibly compromised from various diagenetic processes (see above section 5.1) that can lead to some variability within the recorded $\delta^{34}S_{CAS}$ values, we performed a series of sensitivity tests allowing for some degree of overprinting of primary $\delta^{34}S_{CAS}$ values (Fig. S4–S6). These tests reveal that our fundamental conclusions of decreased seafloor euxinia do not change within a range of reasonable $\delta^{34}S_{CAS}$ variations and possible diagenetic overprinting, but simply affects estimated ranges of total seafloor euxinia. Through careful sample selection and laboratory treatment (i.e. preference of less permeable, low porosity micrite over pack/grainstone, careful extraction procedures to avoid pyrite oxidation) we have generated robust $\delta^{34}S_{CAS}$ datasets that are in good agreement with correlative and previously published $\delta^{34}S_{CAS}$ datasets (Jones and Fike, 2013; Present et al., 2015). However, it is important to acknowledge that diagenetic overprints are still possible but given the results of our sensitivity tests, agreement of trends among sections, and large-scale (>5‰) trends within a section these secondary processes cannot be the primary mechanisms responsible for the major trends in data recorded from these study sites. Ultimately these model results have produced conservative estimates for the extent of seafloor euxinia in the Late Ordovician oceans.

390

391 *5.3 Late Ordovician cascade of redox, environmental, and biotic change*

392 The negative excursion in $\delta^{34}S_{CAS}$ recorded from the late Katian is interpreted to indicate a reduction in global
393 euxinia, which is counter to the occurrence of undifferentiated "anoxic" black shales (i.e. anoxic, ferruginous, or
394 euxinic) found at many locations across the globe during this interval (Melchin et al., 2013). Our I/(Ca+Mg) trends
395 indicate that sub-oxic to anoxic conditions were locally pervasive at least in the sections we studied and by inference
396 may have been widespread in the late Katian oceans and persisted into the Hirnantian. The explanation for this
397 apparent contradiction may lie with the fact that iodine and sulfur respond to different types of reducing conditions,
398 with iodine responding to changes in redox near O_2 reduction (i.e., non-sulfidic anoxia), while sulfate reduction
399 occurs in more reduced settings further down the redox ladder (Froelich et al., 1978; Rue et al., 1997; Lu et al.,
400 2010). Additionally, these two proxies reflect different spatiotemporal relationships, with iodine reflecting local
401 water-column conditions, while $\delta^{34}S_{CAS}$ values record changes in sulfur cycling in the global oceans. In the
402 discussion that follows we focus on this new level of paleoredox specificity for the Late Ordovician oceans in the
403 context of coincident changes in the environment, eustatic sea level, and the marine biosphere.

404 Significant changes in local and global marine redox conditions began in the late Katian and were coincident
405 with high sea level, elevated sea surface temperatures (SSTs), and generally high levels of marine biodiversity
406 (Finney et al., 1999; Haq and Schutter, 2008; Trotter et al., 2008; Rasmussen and Harper, 2011; Finnegan et al.,
407 2011). There is growing evidence from clumped oxygen isotopes and conodont palaeothermometry that global
408 average SSTs began declining in the latest Katian with the initiation of Gondwanan ice sheet expansion (Trotter et
409 al., 2008; Finnegan et al., 2011). This relationship suggests that the negative $\delta^{34}S_{CAS}$ excursion and the implied
410 changes in global average temperature were initiated by the intensification of thermohaline circulation as a result of
411 increased deep-water formation around Gondwanan margins, consistent with sedimentary indicators of upwelling in
412 the Monitor Range section (i.e., bedded cherts and phosphates; Fig. 2) (Pope and Steffen, 2003). Increased
413 thermohaline circulation would have led to cooler globally averaged SSTs and increased renewal of dissolved deep
414 marine O_2, thus ventilating portions of previously euxinic environments along continental margins, shifting the
415 sulfidic chemocline deeper and likely into the sediments in many regions. The ultimate result was a reduced global
416 pyrite burial flux. Thus, euxinic water column conditions may have decreased globally in the latest Katian.
417 However, widespread sulfidic sediment pore waters may help explain the mild enrichments in molybdenum

concentrations and iron speciation records of anoxic, sulfide limited, water-column conditions leading into the Hirnantian as recorded in black shales/deep basinal settings on Laurentia, Baltica, Avalonia, and peri-Gondwana (Hammarlund et al., 2012; Hardisty et al., 2018).

The collective data suggest that a combination of cooling temperatures, reduction of habitable space on shelves and in epeiric seaways due to eustatic sea-level fall (Fig. S3), and our new evidence for possibly widespread non-sulfidic anoxic marine conditions in many local basins culminated in the first LOME pulse near the Katian-Hirnantian boundary. Consistent with this hypothesis, the first appearance of bedded chert in the Monitor Range section, suggesting an increase in local upwelling, coincides with indicators of local sea-level fall (Finney et al., 1997) and expansion of a local OMZ recorded in a drop in I/(Ca+Mg). There is also evidence within previously published bulk nitrogen data (LaPorte et al., 2009) for a shift toward more reducing conditions. This data shows a trend to lighter $\delta^{15}N$ values after our I/(Ca+Mg) ratios drop to near 0 μmol/mol (Fig. 4D) where it is attributed to a local increase in denitrification. Denitrification occurs after iodine reduction on the redox ladder (Lu et al., 2010), consistent with the observed relationship to our iodine data. Together these local redox proxies suggest a progressive loss of oxygen in this local environment prior to the Katian-Hirnantian boundary. Although many Hirnantian localities show evidence of locally reducing conditions, the anomalously high I/(Ca+Mg) ratios recorded from western Anticosti Island are likely due to lowered local sea level allowing for changes in surface currents and nutrient dynamics. The net result was well-oxygenated conditions in very shallow waters that supported patch reef environments in this region. Given the similarities in the iodine data across multiple basins and our inferred global signatures in $\delta^{34}S_{CAS}$, we suggest that euxinia likely decreased globally while, paradoxically, less severe anoxia expanded globally in shallow settings thus non-sulfidic anoxia impacted marine life leading into the first LOME pulse. This reduction in euxinic conditions may be attributed to the observed global cooling of surface waters and subsequent increased solubility of O_2, combined with enhanced thermohaline circulation, thus ventilating previously euxinic portions of Late Ordovician oceans. This enhanced ocean circulation may have in turn intensified local upwelling around continental margins throughout the globe, thus leading to more local primary productivity, enhancing global carbon burial and local anoxia, as evidenced by I/(Ca+Mg) trends. These climatic and oceanographic conditions during the late Katian–Hirnantian may have provided a unique balance that resulted in expansion of anoxic non-sulfidic water masses, but the increased oxygen solubility and circulation may have

prevented these water masses from being pervasively euxinic. Ultimately, these marine redox conditions would have had a major impact on marine life in productive continental margins and remaining shallow seaways.

Changes in global marine redox conditions associated with eustatic sea-level rise have been invoked as a causal mechanism for the second LOME pulse in the late Hirnantian (within the *M. persculptus* graptolite biozone) (Harper et al., 2014). As Gondwanan ice sheets melted and the late Hirnantian climate warmed (Finnegan et al., 2011), marine stratification and chemocline migration during eustatic sea-level rise likely played an important role in the second LOME pulse. The $\delta^{238}U$ records from carbonates on western Anticosti Island (Bartlett et al., 2018)—along with $\delta^{98}Mo$ and $\delta^{238}U$ data, Mo concentrations, and iron speciation from organic-rich shale successions (Hammarlund et al., 2012; Zhou et al., 2015; Zou et al., 2018; Stockey et al., 2020)—indicate a return to widespread reducing conditions in global oceans during this time. Our iodine and sulfur isotope datasets are consistent with a shift to more reducing conditions. Specifically, late Hirnantian–early Silurian I/(Ca+Mg) values indicate local anoxia at all three sections, and $\delta^{34}S_{CAS}$ profiles from all sites trend positively by ~ 7‰ (Fig. 5), indicating a return to increased global pyrite burial. Increased reducing conditions along continental margins during this time would have largely tracked eustatic sea-level rise, warming sea surface temperatures would have led to decreased O_2 solubility and circulation. As OMZs expanded from deep shelf/slope to shallower areas on the continental shelf during the late Hirnantian–early Silurian this increased the overall areal extent of seafloor overlain by anoxic and euxinic bottom waters.

6. Conclusions

Paired iodine and sulfur isotope geochemistry reveal new spatiotemporal relationships between marine non-sulfidic anoxia and euxinia associated with the Late Ordovician Mass Extinction. Our I/(Ca+Mg) ratios are low throughout this time interval in all sections, except for a set of high values (average of 6 μmol/mol) recorded from the shallow patch reef facies on western Anticosti Island. At the same time, our new $\delta^{34}S_{CAS}$ records show a large negative excursion of ~ 10‰ magnitude over the late Katian–Hirnantian. Modeling of these $\delta^{34}S_{CAS}$ records suggests that the negative excursion was driven by moderate decreases in the pyrite burial rates combined with modest increases in weathering. Our model also suggests reductions of global seafloor euxinic conditions by ~ 3% from the late Katan into the Hirnantian. This is a maximum estimate, but it is consistent with recent models of Hirnantian to early Silurian global redox-based on other proxy data (Bartlett et al., 2018; Stockey et al., 2020). Importantly, this transition does not preclude the possibility of increasing oxygen deficiency as recorded in iodine data in marginal

473 settings due to enhanced upwelling as seen in the Monitor Range. Additional data from redox-sensitive elements are
474 needed from multiple paleobasins to constrain the extent of these non-sulfidic reducing conditions.
475 In sum, our multiproxy data and modeling indicate widespread ventilation of marine environments
476 followed by enhanced weathering during the late Katian–early Hirnantian. This sequence of events likely resulted
477 from enhanced thermohaline circulation and growth of Gondwanan ice sheets that cooled sea surface temperatures
478 and potentially increased deeper ocean oxygenation, therefore reducing euxinic conditions in the global oceans.
479 However, non-sulfidic anoxic conditions remained pervasive throughout shallow shelf settings due to attendant
480 increases in productivity resulting from increased upwelling and ocean circulation. These relationships indicate that
481 a unique combination of reducing marine conditions, climatic cooling, and glacioeustacy led to the first LOME
482 pulse. Subsequently, deglacial eustatic sea-level rise during the late Hirnantian that coincided with warming
483 temperatures, deoxygenation, and decreased ocean circulation led to an expansion of global euxinic conditions,
484 broadly coincident with the second LOME pulse. Our study sheds new light on the possibility of a complex and
485 evolving redox landscape reflecting the interplay of multiple interrelated controls—with severe biotic turnover as a
486 consequence. More generally, these results hint at the improved perspective that can come by integrating multiple
487 local and global proxies from a wide distribution of locations.

488 ## Acknowledgments

489 N.P.K would like to thank Chelsie Bowman, Randall Funderburk, Anders Lindskog, and Westly Owings for their
490 support and/or assistance in sample collection and preparation. B.C.G. would like to thank Charles Gill for
491 assistance in sample collection in Nevada. We thank Dimitri Kaljo for access and assistance in sample collection of
492 the Kardla drill core. This research was funded by the American Chemical Society Petroleum Research Fund (grant
493 ACS-PRF# 57487-DNI2 to S.A.Y.) and the National Science Foundation (EAR-1748635 to S.A.Y. and J.D.O. and
494 EAR-0418270 to T.W.L.). Additional funds were provided by the NASA Astrobiology Institute under Cooperative
495 Agreement No. NNA15BB03A issued through the Science Mission Directorate (to T.W.L.). This work was in part
496 performed at the National High Magnetic Field Laboratory, which is supported by the National Science Foundation
497 Cooperative Agreement No. DMR-1157490 and the State of Florida. The authors declare no conflict of interest.

498 ## Data Availability Statement

All data used in this study is made available in this article and its supporting information. All geochemical data processed in this study will be submitted to the EarthChem Database.

References

Ahm, A.S.C., Bjerrum, C.J., Blättler, C.L., Swart, P.K., and Higgins, J.A., 2018, Quantifying early marine diagenesis in shallow-water carbonate sediments: Geochimica et Cosmochimica Acta, v. 236, p. 140–159, doi:10.1016/j.gca.2018.02.042.

Bartlett, R., Elrick, M., Wheeley, J.R., Polyak, V., Desrochers, A., and Asmerom, Y., 2018, Abrupt global-ocean anoxia during the Late Ordovician – early Silurian detected using uranium isotopes of marine carbonates: Proceedings of the National Academy of Sciences, v. 115, p. 5896–5901, doi:10.1073/pnas.1802438115.

Brenchley, P.J., Carden, G.A., Hints, L., Kaljo, D., Marshall, J.D., Martma, T., Meidla, T., and Nõlvak, J., 2003, High-resolution stable isotope stratigraphy of Upper Ordovician sequences: Constraints on the timing of bioevents and environmental changes associated with mass: Geological Society of America Bulletin, v. 115, p. 89–104, doi:10.1130/0016-7606(2003)115<0089.

Brenchley, P.J., Marshall, J.D., and Underwood, C.J., 2001, Do all mass extinctions represent an ecological crisis? Evidence from the Late Ordovician: Geological Journal, v. 36, p. 329–340, doi:10.1002/gj.880.

Burke, A. et al., 2018, Sulfur isotopes in rivers: Insights into global weathering budgets, pyrite oxidation, and the modern sulfur cycle: Earth and Planetary Science Letters, v. 496, p. 168–177, doi:10.1016/j.epsl.2018.05.022.

Desrochers, A., Farley, C., Achab, A., Asselin, E., and Riva, J.F., 2010, A far-field record of the end Ordovician glaciation : The Ellis Bay Formation , Anticosti Island , Eastern Canada: Palaeogeography, Palaeoclimatology, Palaeoecology, v. 296, p. 248–263, doi:10.1016/j.palaeo.2010.02.017.

Finnegan, S., Bergmann, K., Eiler, J.M., Jones, D.S., Fike, D.A., Eisenman, I., Hughes, N.C., Tripati, A.K., and Fischer, W.W., 2011, The Magnitude and Duration of Late Ordovician-Early Silurian Glaciation: Science, v. 331, p. 903–906, doi:10.1126/science.1200803.

Finney, S.C., Berry, W.B.N., Cooper, J.D., Ripperdan, R.L., Jacobson, S.R., Québec, C.G. De, Canada, G. V, and Noble, P.J., 1999, Late Ordovician mass extinction : A new perspective from stratigraphic sections in central Nevada: Geology, p. 215–218.

Finney, S.C., Cooper, J.D., and Berry, W.B.N., 1997, Late Ordovician Mass Extinction: Sedimentologic,

526 Cyclostratigraphic, and Biostratigraphic Records from Platform and Basin Successions, Central Nevada:
527 Brigham Young University Geology Studies, v. 42, p. 79–103.
528 Froelich, P.N., Klinkhammer, G.P., Bender, M.L., Luedtke, N.A., Heath, G.R., Cullen, D., Dauphin, P., Hammond,
529 D., and Hartman, B., 1978, Early oxidation of organic matter in pelagic sediments of the eastern equatorial
530 Atlantic : suhoxic diagenesis: Geochimica et Cosmochimica Acta, v. 43, p. 1075–1090.
531 Ghienne, J.F. et al., 2014, A Cenozoic-style scenario for the end-ordovician glaciation: Nature Communications, v.
532 5, doi:10.1038/ncomms5485.
533 Gill, B.C., Lyons, T.W., and Frank, T.D., 2008, Behavior of carbonate-associated sulfate during meteoric diagenesis
534 and implications for the sulfur isotope paleoproxy: Geochimica et Cosmochimica Acta, v. 72, p. 4699–4711,
535 doi:10.1016/j.gca.2008.07.001.
536 Goldman, D., Sadler, P.M., and Leslie, S.A., 2020, Chapter 20 – The Ordovician Period: BV, 489–523 p.,
537 doi:10.1016/B978-0-444-63798-7.00020-3.
538 Gomes, M.L., and Hurtgen, M.T., 2015, Sulfur isotope fractionation in modern euxinic systems: Implications for
539 paleoenvironmental reconstructions of paired sulfate-sulfide isotope records: Geochimica et Cosmochimica
540 Acta, v. 157, p. 39–55, doi:10.1016/j.gca.2015.02.031.
541 Hammarlund, E.U., Dahl, T.W., Harper, D.A.T., Bond, D.P.G., Nielsen, A.T., Bjerrum, C.J., Schovsbo, N.H.,
542 Schönlaub, H.P., Zalasiewicz, J.A., and Canfield, D.E., 2012, A sulfidic driver for the end-Ordovician mass
543 extinction: Earth and Planetary Science Letters, v. 331–332, p. 128–139, doi:10.1016/j.epsl.2012.02.024.
544 Haq, B.U., and Schutter, S.R., 2008, A Chronology of Paleozoic Sea-Level Changes: Science, v. 322, p. 64–68,
545 doi:10.1126/science.1161648.
546 Hardisty, D.S. et al., 2017, Perspectives on Proterozoic surface ocean redox from iodine contents in ancient and
547 recent carbonate: Earth and Planetary Science Letters, v. 463, p. 159–170, doi:10.1016/j.epsl.2017.01.032.
548 Hardisty, D.S., Horner, T.J., Evans, N., Moriyasu, R., Babbin, A.R., Wankel, S.D., Moffett, J.W., and Nielsen, S.G.,
549 2020, Limited iodate reduction in shipboard seawater incubations from the Eastern Tropical North Pacific
550 oxygen deficient zone: Earth and Planetary Science Letters, v. 554, p. 116676,
551 doi:10.1016/j.epsl.2020.116676.
552 Hardisty, D.S., Lu, Z., Planavsky, N.J., Bekker, A., Philippot, P., Zhou, X., and Lyons, T.W., 2014, An iodine
553 record of Paleoproterozoic surface ocean oxygenation: Geology, v. 42, p. 619–622, doi:10.1130/G35439.1.

554 Hardisty, D.S., Lyons, T.W., Riedinger, N., Isson, T.T., Owens, J.D., Aller, R.C., Rye, D.M., Planavsky, N.J., Asael,
555 D.A.N., and Johnston, D.T., 2018, An Evaluation of Sedimentary Molybdenum and Iron as Proxies for Pore
556 Fluid Paleoredox Conditions: American Journal of Science, v. 318, p. 527–556, doi:10.2475/05.2018.04.
557 Harper, D.A.T., Hammarlund, E.U., and Rasmussen, C.M.Ø., 2014, End Ordovician extinctions: A coincidence of
558 causes: Gondwana Research, v. 25, p. 1294–1307, doi:10.1016/j.gr.2012.12.021.
559 Horita, J., Zimmermann, H., and Holland, H.D., 2002, Chemical evolution of seawater during the Phanerozoic:
560 Geochimica et Cosmochimica Acta, v. 66, p. 3733–3756, doi:10.1016/S0016-7037(01)00884-5.
561 Hu, D., Zhang, X., Zhou, L., Finney, S.C., and Liu, Y., 2017, 87 Sr / 86 Sr evidence from the epeiric Martin Ridge
562 Basin for enhanced carbonate weathering during the Hirnantian: Scientific Reports, p. 1–7,
563 doi:10.1038/s41598-017-11619-w.
564 Jones, D.S., Brothers, R.W., Ahm, A.C., Slater, N., Higgins, J.A., and Fike, D.A., 2020, Sea level, carbonate
565 mineralogy, and early diagenesis controlled δ 13C records in Upper Ordovician carbonates: Geology, v. 48, p.
566 1–6, doi:10.1130/G46861.1/4902172/g46861.pdf.
567 Jones, D.S., Creel, R.C., and Rios, B.A., 2016, Carbon isotope stratigraphy and correlation of depositional
568 sequences in the Upper Ordovician Ely Springs Dolostone , eastern Great Basin , USA: Palaeogeography,
569 Palaeoclimatology, Palaeoecology, v. 458, p. 85–101, doi:10.1016/j.palaeo.2016.01.036.
570 Jones, D.S., and Fike, D.A., 2013, Dynamic sulfur and carbon cycling through the end-Ordovician extinction
571 revealed by paired sulfate–pyrite δ34S: Earth and Planetary Science Letters, v. 363, p. 144–155,
572 doi:10.1016/j.epsl.2012.12.015.
573 Jones, D.S., Fike, D.A., Finnegan, S., Fischer, W.W., Schrag, D.P., and McCay, D., 2011, Terminal Ordovician
574 carbon isotope stratigraphy and glacioeustatic sea-level change across Anticosti Island (Quebec, Canada):
575 Geological Society of America Bulletin, v. 123, p. 1645–1664, doi:10.1130/B30323.1.
576 Kaljo, D., Hints, L., Hints, O., Männik, P., Martma, T., and Nõlvak, J., 2011, Katian prelude to the Hirnantian (Late
577 Ordovician) mass extinction: A Baltic perspective: Geological Journal, v. 46, p. 464–477,
578 doi:10.1002/gj.1301.
579 Kaljo, D., Hints, L., Martma, T., and Nõlvak, J., 2001, Carbon isotope stratigraphy in the latest Ordovician of
580 Estonia: Chemical Geology, v. 175, p. 49–59, doi:10.1016/S0009-2541(00)00363-6.
581 Kiipli, E., and Kiipli, T., 2020, Hirnantian sea-level changes in the Baltoscandian Basin, a review: Palaeogeography,

582 Palaeoclimatology, Palaeoecology, v. 540, p. 109524, doi:10.1016/j.palaeo.2019.109524.
583 Kump, L.R., Arthur, M.A., Patzkowsky, M.E., Gibbs, M.T., Pinkus, D.S., and Sheehan, P.M., 1999, A weathering
584 hypothesis for glaciation at high atmospheric pCO2 during the Late Ordovician: Palaeogeography,
585 Palaeoclimatology, Palaeoecology, v. 152, p. 173–187, doi:10.1016/S0031-0182(99)00046-2.
586 Kurtz, A.C., Kump, L.R., Arthur, M.A., Zachos, J.C., and Paytan, A., 2003, Early Cenozoic decoupling of the global
587 carbon and sulfur cycles: Paleoceanography, v. 18, doi:10.1029/2003PA000908.
588 Lang, X., Tang, W., Ma, H., and Shen, B., 2020, Local environmental variation obscures the interpretation of pyrite
589 sulfur isotope records: Earth and Planetary Science Letters, v. 533, p. 1–7, doi:10.1016/j.epsl.2019.116056.
590 LaPorte, D.F., Holmden, C., Patterson, W.P., Loxton, J.D., Melchin, M.J., Mitchell, C.E., Finney, S.C., and Sheets,
591 H.D., 2009, Local and global perspectives on carbon and nitrogen cycling during the Hirnantian glaciation:
592 Palaeogeography, Palaeoclimatology, Palaeoecology, v. 276, p. 182–195, doi:10.1016/j.palaeo.2009.03.009.
593 Lu, W. et al., 2018, Late inception of a resiliently oxygenated upper ocean: Science, v. 177, p. 174–177,
594 doi:10.1126/science.aar5372.
595 Lu, Z., Jenkyns, H.C., and Rickaby, R.E.M., 2010, Iodine to calcium ratios in marine carbonate as a paleo-redox
596 proxy during oceanic anoxic events: Geology, v. 38, p. 1107–1110, doi:10.1130/G31145.1.
597 Melchin, M.J., Mitchell, C.E., Holmden, C., and Štorch, P., 2013, Environmental changes in the late ordovician-
598 early silurian: Review and new insights from black shales and nitrogen isotopes: Bulletin of the Geological
599 Society of America, v. 125, p. 1635–1670, doi:10.1130/B30812.1.
600 Murphy, M.A., Dunham, J.B., Berry, W.B.N., and Matti, J.C., 1979, Late Llandovery Unconformity in Central
601 Nevada: Brigham Young University Geology Studies, v. 26, p. 21–36.
602 Neretin, L.N., Volkov, I.I., Böttcher, M.E., and Grinenko, V.A., 2001, A sulfur budget for the Black Sea anoxic
603 zone: Deep-sea Research I, v. 48, p. 2569–2593.
604 Pasquier, V., Bryant, R.N., Fike, D.A., and Halevy, I., 2021, Strong local, not global, controls on marine pyrite
605 sulfur isotopes: Science Advances, v. 7, p. 1–11.
606 Pope, M.C., and Steffen, J.B., 2003, Widespread, prolonges late Middle to Late Ordovician upwelling in North
607 America: a proxy record of glaciation? Geology, v. 31, p. 63–66, doi:10.1130/0091-7613-31.1.e28.
608 Present, T.M., Paris, G., Burke, A., Fischer, W.W., and Adkins, J.F., 2015, Large Carbonate Associated Sulfate
609 isotopic variability between brachiopods, micrite, and other sedimentary components in Late Ordovician

610 strata: Earth and Planetary Science Letters, v. 432, p. 187–198, doi:10.1016/j.epsl.2015.10.005.
611 Rasmussen, C.M.Ø., and Harper, D.A.T., 2011, Did the amalgamation of continents drive the end Ordovician mass
612 extinctions ? Palaeogeography, Palaeoclimatology, Palaeoecology, v. 311, p. 48–62,
613 doi:10.1016/j.palaeo.2011.07.029.
614 Rasmussen, C.M.Ø., Kröger, B., Nielsen, M.L., and Colmenar, J., 2019, Cascading trend of Early Paleozoic marine
615 radiations paused by Late Ordovician extinctions: Proceedings of the National Academy of Sciences, p. 1–7,
616 doi:10.1073/pnas.1821123116.
617 Reinhard, C.T., Planavsky, N.J., Robbins, L.J., Partin, C.A., Gill, B.C., Lalonde, S. V., Bekker, A., Konhauser,
618 K.O., and Lyons, T.W., 2013, Proterozoic ocean redox and biogeochemical stasis: Proceedings of the National
619 Academy of Sciences, v. 110, p. 5357–5362, doi:10.1073/pnas.1208622110.
620 Rue, E.L., Smith, G.J., and Bruland, K.W., 1997, The response of trace element redox couples to suboxic conditions
621 in the water column: Deep-sea Research I, v. 44, p. 113–134.
622 Sim, M.S., 2019, Effect of sulfate limitation on sulfur isotope fractionation in batch cultures of sulfate reducing
623 bacteria: Geosciences Journal, v. 23, p. 687–694.
624 Stockey, R.G., Cole, D.B., Planavsky, N.J., Loydell, D.K., Frýda, J., and Sperling, E.A., 2020, Persistent global
625 marine euxinia in the early Silurian: Nature Communications, v. 11, p. 1804, doi:10.1038/s41467-020-15400-
626 y.
627 Swart, P.K., and Oehlert, A.M., 2018, Revised interpretations of stable C and O patterns in carbonate rocks resulting
628 from meteoric diagenesis: Sedimentary Geology, v. 364, p. 14–23, doi:10.1016/j.sedgeo.2017.12.005.
629 Toyama, K., Paytan, A., Sawada, K., and Hasegawa, T., 2020, Sulfur isotope ratios in co-occurring barite and
630 carbonate from Eocene sediments : A comparison study: Chemical Geology, v. 535, p. 119454,
631 doi:10.1016/j.chemgeo.2019.119454.
632 Trotter, J.A., Williams, I.S., Barnes, C.R., Lécuyer, C., and Nicoll, R.S., 2008, Did Cooling Oceans Trigger
633 Orovician Biodiversification? Evidence from Conodont Thermometry: Science, v. 321, p. 550–554,
634 doi:10.1126/science.1155814.
635 Yao, W., Paytan, A., Griffith, E.M., Martínez-ruiz, F., Markovic, S., and Wortmann, U.G., 2020, A revised seawater
636 sulfate S-isotope curve for the Eocene: Chemical Geology, v. 532, p. 119382,
637 doi:10.1016/j.chemgeo.2019.119382.

638 Young, S.A., Saltzman, M.R., Ausich, W.I., Desrochers, A., and Kaljo, D., 2010, Did changes in atmospheric CO2
639 coincide with latest Ordovician glacial–interglacial cycles? Palaeogeography, Palaeoclimatology,
640 Palaeoecology, v. 296, p. 376–388, doi:10.1016/j.palaeo.2010.02.033.
641 Zhou, L., Algeo, T.J., Shen, J., Hu, Z.F., Gong, H., Xie, S., Huang, J.H., and Gao, S., 2015, Changes in marine
642 productivity and redox conditions during the Late Ordovician Hirnantian glaciation: Palaeogeography,
643 Palaeoclimatology, Palaeoecology, v. 420, p. 223–234, doi:10.1016/j.palaeo.2014.12.012.
644 Zou, C., Qiu, Z., Poulton, S.W., Dong, D., Wang, H., Chen, D., Lu, B., Shi, Z., and Tao, H., 2018, Ocean euxinia
645 and climate change “double whammy” drove the Late Ordovician mass extinction: Geology, v. 46, p. 535–
646 538, doi:10.1130/G40121.1.
647